Effect of pressure on the properties of a NASICON Li$_{1.3}$Al$_{0.3}$Ti$_{1.7}$(PO$_4$)$_3$ nanofiber solid electrolyte

Andrea La Monaca,[ab] Gabriel Girard,[a] Sylvio Savoie,[a] Hendrix Demers,[a] Giovanni Bertoni,[cd] Sergey Krachkovskiy,[a] Sergio Marras,[e] Enrico Mugnaioli,[f] Mauro Gemmi,[f] Daniele Benetti,[b] Ashok Vijh,[a] Federico Rosei[b] and Andrea Paolella*[a]

We report the effect of pressure on a membrane made of dense electrospun NASICON-like Li$_{1.3}$Al$_{0.3}$Ti$_{1.7}$(PO$_4$)$_3$ (LATP). The properties and performance of the pressed LATP nanofibers were investigated and compared with those of pristine LATP nanofibers. While the applied pressure affects the purity and homogeneity of LATP, it is beneficial for ionic transport across the solid electrolyte. The presence of impurity phases as well as the decrease of porosity results in a two order of magnitude higher ionic conductivity at room temperature (3 × 10^{-5} S cm^{-1}) which is promising to replace bulk NASICON materials in energy storage devices.

Introduction

During the last few decades one-dimensional (1D) structures such as fibers, wires and rods have been widely investigated to develop anodes, cathodes, separators, and electrolytes with superior properties to enhance the performance of lithium-ion batteries and other energy technologies.[1–12] Nevertheless, the quest for a technology with improved safety and better performance that is capable of replacing lithium-ion batteries is ongoing.[13,14] One of the best candidates is the all-solid-state lithium battery (ASSLB), which is characterized by a solid electrolyte, made of an inorganic, polymeric or composite material and which uses metallic lithium as anode.[15,16] Recently ceramic 1D structures have been widely investigated for developing novel solid electrolytes for ASSLBs.[17] Specifically, nanofibers and nanowires have been mainly employed as inorganic fillers for polymer-based composite electrolytes, exhibiting better lithium ion conduction and mechanical properties compared to their nanoparticle counterparts.[18–27] Additionally, they have been studied as basis to develop fully ceramic pellets, resulting in denser and better conductive electrolytes.[28] A good understanding and use of nanocrystalline structures is crucial for the development of future battery technologies.[29–31]

Several materials with high ionic conductivity have been synthesized as elongated structures and used in various battery technologies, such as perovskite-type Li$_{0.33}$La$_{0.557}$TiO$_3$,[18–22,28] garnet-type Li$_7$La$_3$Zr$_2$O$_{12}$ (ref. 23–27 and 32) and NASICON (Na super ionic conductor)-type Li$_{1.4}$Al$_{0.4}$Ti$_{1.6}$(PO$_4$)$_3$ and Li$_{1.5}$Al$_{0.5}$Ge$_{1.5}$(PO$_4$)$_3$.[33,34]

NASICON materials are one of the most promising solid electrolyte families for ASSLBs because of their high ionic conductivity and stability in ambient conditions. Li$_{1+x}$Al$_x$-Ti$_{2-x}$(PO$_4$)$_3$ is probably the most representative structure of Li-based NASICON materials, as it presents the highest ionic conductivity of the family and can be synthesized from easily processable and low-cost materials. Its high ionic conductivity is mainly due to two different factors: (1) the large ionic radius of Ti^{4+} (0.605 A) increases the size of the bottleneck in the lithium ion migration by distorting the network; (2) the partial aliovalent substitution of Ti^{4+} by Al^{3+} increases the concentration of lithium ions in the structure, as well as their mobility.[35,36] While lithium ions preferentially occupy the M1 site in the LiTi$_2$(PO$_4$)$_3$-like structure, the increase of lithium concentration due to the Al doping promotes the occupation of M3 sites. A partial occupation of both sites proved to be crucial for fast lithium conduction.[35,37] Several recent studies demonstrated the potential applicability of Li$_{1+x}$Al$_x$Ti$_{2-x}$(PO$_4$)$_3$ as solid electrolyte in both lithium metal batteries and lithium air batteries.[38–40] Lancel et al. reported the synthesis of ceramic Li$_{1.4}$Al$_{0.4}$Ti$_{1.6}$(-PO$_4$)$_3$ fibers by electrospinning and subsequent calcination, which have been then used as inorganic component into a hybrid membrane for lithium–air batteries.[33] The ionic

^{a}Centre D'excellence en Électrification des Transports et Stockage D'énergie, Hydro-Québec, 1806 Boulevard Lionel-Boulet, Varennes, Québec J3X 1S1, Canada. E-mail: paolella.andrea2@hydroquebec.com

^{b}Centre Énergie, Matériaux et Télécommunications, Institut National de la Recherche Scientifique, 1650 Boulevard Lionel-Boulet, Varennes, Québec J3X 1S2, Canada

^{c}IMEM-CNR, Parco Area delle Scienze 37/A, Parma 43124, Italy

^{d}CNR – Istituto Nanoscienze, Via Campi 213/A, Modena 41125, Italy

^{e}Istituto Italiano di Tecnologia, Via Morego 30, Genova 16163, Italy

^{f}Istituto Italiano di Tecnologia, Center for Nanotechnology Innovation @NEST, Piazza San Silvestro 12, Pisa 56127, Italy

conductivity reported for the ceramic membrane (3×10^{-7} S cm^{-1}) is significantly lower than the bulk conductivity value previously achieved for the same structure (10^{-4} S cm^{-1}),[41] because of the typical high porosity of electrospun materials.

Here we adapt the synthetic procedure employed by Lancel *et al.* to achieve the most conductive Li$_{1.3}$Al$_{0.3}$Ti$_{1.7}$(PO$_4$)$_3$ stoichiometry. With the aim of reducing the porosity of the ceramic membrane, the effect of applying a 150 MPa pressure to the electrospun membrane, prior to the heat treatment has been investigated. Here we report how the pressing process affects the morphology of the membrane as well as the structure and the physico/chemical properties of the ceramic material. Despite the presence of some impurity phases and a less homogeneous substitution of Ti^{4+} by Al^{3+}, the pressed LATP nanofibers showed an increased ionic conductivity and a much smaller activation energy compared to pristine LATP fibers.

Experimental

Materials

Lithium nitrate (LiNO$_3$, reagent grade, Sigma-Aldrich), aluminum nitrate nonahydrate (Al(NO$_3$)$_3$·9H$_2$O, ≥98%, Sigma-Aldrich), titanium butoxide (C$_{16}$H$_{36}$O$_4$Ti, 97%, Sigma-Aldrich), and phenylphosphonic acid (PPA) (C$_6$H$_7$O$_3$P, 98%, Sigma-Aldrich) were used as precursor materials. Poly(vinylidene fluoride-*co*-hexafluoropropene) (PVDF–HFP) (Sigma Aldrich) was used as polymer carrier for the electrospinning process. *N,N*-Dimethylformamide (DMF) (C$_3$H$_7$NO, anhydrous, 99.8%, Sigma-Aldrich), tetrahydrofuran (THF) (C$_4$H$_8$O, anhydrous, ≥99.9%, Sigma-Aldrich) and acetylacetone (C$_5$H$_8$O$_2$, Sigma-Aldrich, ≥99%) were used to dissolve the materials above.

Synthesis of LATP nanofibers

The preparation process, based on sol–gel principles, is shown in Fig. 1. In a typical procedure, 160 mg of PVDF–HFP and stoichiometric amounts of lithium nitrate (3.64 mmol), aluminum nitrate (0.84 mmol), and PPA (8.40 mmol) were added to 8 mL of DMF : THF (1 : 1 v/v) and dissolved by magnetically stirring the solution overnight. A stoichiometric amount of titanium butoxide (4.76 mmol) was then added to the main solution, after being previously stabilized in 2 equivalents of acetylacetone. For the sake of reproducibility, all the steps have been carried out inside a dry room. The viscous sol was then loaded in a plastic syringe and electrospun by a NanoNC eSrobot machine by using a 20 μL min^{-1} flow rate and applying 15 kV to the needle by means of a high voltage power supply. The fibers were deposited onto a cylindrical rotating collector (300 rpm rotation angular speed) wrapped in aluminum foil and connected to a secondary high-voltage power supply, to apply −2 kV to favor the fiber deposition. A distance of 10 cm between needle and collector was used to let the solvents evaporate. After about 6 hours, a dry white yellowish membrane was collected and dried at 75 °C overnight to remove potential solvent traces.

Several circular samples with 20 mm diameter were cut from the dried membrane using a puncher and stacked to achieve a suitable thickness (150–200 μm). The stacked samples were
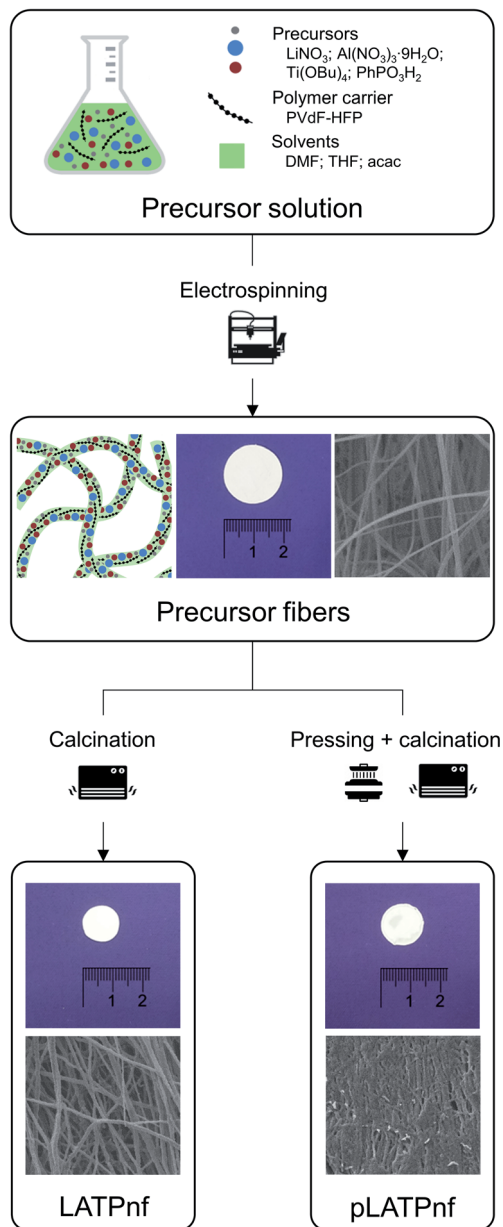

Fig. 1 Schematic illustration of the synthesis process of LATP pressed fibers.

then pressed using a hydraulic press at 150 MPa to reduce their porosity and calcined at 850 °C for 2 h with a heating rate of 5 °C min^{-1} to achieve pressed LATP nanofibers, hereafter referred to as pLATPnf.

Characterization

Porosity values of LATPnf and pLATPnf samples were calculated using the following equation:

$$p\ (\%) = 100 - \left[\left(\frac{wv}{d_{\text{th}}} \right) \times 100 \right]$$

where w and v are the weight and the volume of the sample respectively, and d_{th} is the theoretical density of LATP (estimated to be equal to 2.9 g cm^{-3}).

X-ray diffraction (XRD) patterns were acquired using a Rigaku SmartLab X-ray diffractometer equipped with a 9 kW Cu K$_\alpha$ rotating anode (operating at 40 kV and 150 mA) and D\teX Ultra 1D silicon strip detector. The diffraction patterns were collected at room temperature in the Bragg–Brentano geometry over the angular range: $2\theta = 10°-100°$, with a step size of $0.01°$. XRD data analysis was carried out using PDXL 2.8.4.0 software from Rigaku.

Scanning electron microscopy (SEM) images and energy-dispersive X-ray spectra (EDS) were acquired using a Hitachi FlexSEM SU1000 scanning electron microscope and a Hitachi SU7000 equipped with an Ultim Max Oxford Instrument EDS at different accelerating voltages (5 kV–15 kV). Prior to the observation with the FlexSEM SU1000, the samples were sputter-coated with a thin layer of gold (*ca.* 3 nm) to increase the electronic conductivity.

[7]Li solid-state Magic Angle Spinning (MAS) NMR spectra were recorded at room temperature in 500 MHz WB Bruker AVANCE NEO NMR spectrometer (Larmor frequency for [7]Li is 194.38 MHz) equipped with 4 mm triple resonance probe. Single pulse NMR experiments were used to acquire MAS NMR spectra at a spinning speed of 2 kHz. 16 scans with $\pi/2$ pulse of 3 μs and relaxation delay of 10 s were collected for each sample. NMR chemical shifts were referred to 1 M LiCl aqueous solutions. NMR spectra were fitted with the Bruker Topspin 4.1 build-in module SOLA.

High-resolution transmission electron microscopy (HRTEM) and high-angle annular dark-field scanning electron microscopy (HAADF-STEM) were carried out using a Thermo Scientific Talos F200S G2 TEM microscope, working at 200 kV.

Three-dimensional electron diffraction (3D ED)[42] data were collected with a Zeiss Libra TEM operating at 120 kV and equipped with a LaB$_6$ source. Data acquisition was performed in STEM mode after defocusing the beam to achieve parallel illumination of the sample. A beam size of about 150 nm in diameter was obtained by inserting a 5 μm C2 condenser aperture.[43] The data was recorded using an ASI Timepix detector, able to register the arrival of single electrons and to deliver a pattern that is virtually background-free. 3D ED data were taken from six fragments belonging to the main trigonal phase. Fragments had a typical pseudo-hexagonal platelet habit and diameter comparable with the beam size. 3D ED data were collected with a precessing beam (precession angle 1°), in fixed steps of 1° and for a total range from 90° to 116°. The camera length was 180 mm, corresponding to a maximum resolution of 0.75 Å. The data was analyzed using ADT3D software.[44] The *ab initio* structure solution was obtained by direct methods implemented in the software SIR2014,[45] using a kinematical approximation: I_{hkl} proportional to F_{hkl}^2.

X-ray photoelectron spectra (XPS) were acquired using a VG Escalab 220i-XL spectrometer equipped with a hemispherical analyzer, applying a Twin Anode X-ray Source. The binding energy was calibrated by reference to the C 1s peak (284.8 eV).

Electrochemical impedance spectroscopy (EIS) was carried out using a BioLogic VMP potentiostat/galvanostat by applying an AC perturbation of 5 mV in a frequency range of 1 MHz–50 mHz from 20 to 80 °C. Prior to EIS measurements, the samples were sputter-coated with a thin layer of Pt on both sides, to improve the electrical contact. They were then placed between stainless steel blocking electrodes in 2032-type coin cells.

Results and discussion

Using a hydraulic press, various loads have been applied to stacked samples of precursor fibers to identify the value at which the porosity is being reduced without compromising fiber morphology and mechanical integrity of the sample during the heat treatment. A trade-off value was identified at 150 MPa, which reduces the porosity of the ceramic sample from 85% to 60% without affecting its integrity and morphology. Applying a pressure higher than 150 MPa results in a denser sample, which is however more prone to fracture during the heat treatment (Fig. S1†). Fractures could arise from a reduced ability to accommodate the decrease in volume, as well as from gaseous side products generated at high temperature trying to escape from the sample. After the pressing step, pLATPnf samples were calcined at 850 °C for 2 h with a heating rate of 5 °C min^{-1}. The selected temperature and time allowed to achieve an almost pure LATP phase with the sought NASICON structure, without compromising the fiber shape. The fibers tend to coalesce when severe heating conditions are used, as already reported.[32] As shown in Fig. 1, the area of the sample has halved during the heating treatment. The observed shrinkage is due to the decomposition and loss of the polymer and organic side products, and to the simultaneous crystallization of LATP.

The results presented and discussed below for pLATPnf are compared to those of non-pressed LATP nanofibers samples, simply referred to as LATPnf, which have been prepared by following the same procedure, except for the pressing step.

SEM images of LATP precursor fibers, LATPnf and pLATPnf are displayed in Fig. 2. The as spun precursor fibers are characterized by a diameter ranging from 700 nm to 2 μm (Fig. 2a). After calcination, the fiber diameter decreased to a range of 0.4–1 μm (Fig. 2b). LATPnf maintained the 1D morphology because the separation of the fibers ensures that crystal growth occurs only inside each single fiber. This also allows to control the crystallites' size by using the fiber confinement as a template. Fig. 2c clearly shows how the pressure applied to pLATPnf greatly decreases the porosity and thus increases the number of contact points among the fibers, which is beneficial for the ionic conductivity of the final material. In terms of morphology, the nanofibers are still easily discernible, and the coalescence is minimized. However, there is almost no spatial separation among the nanofibers, hence crystal growth is not as confined as for LATPnf. Fig. 2d and e show how this affects the final dimension of crystalline domains composing the fibers, ranging from 100 to 250 nm in LATPnf while reaching 600 nm in pLATPnf. A different crystal shape can also be noticed: while LATPnf are composed of cubic-shaped crystallites, typical of the NASICON phase,[46-48] pLATPnf are mostly made of spherical crystallites. These structures were previously observed by Schell *et al.* when temperatures lower than or equal to 800 °C are employed for a 10 h calcination step of sol–gel synthesized LATP. Although the temperature used for pLATPnf is higher
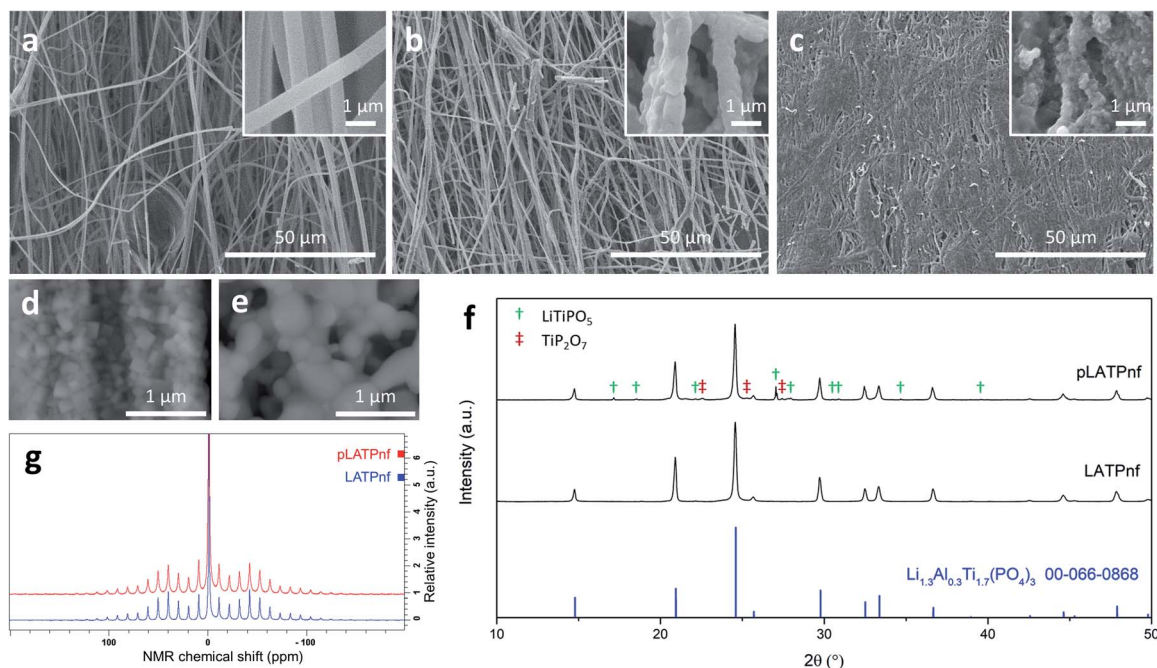
Fig. 2 SEM images of (a) LATP precursor fibers, (b) LATPnf and (c) pLATPnf (corresponding magnification in the inset). High magnification SEM images of crystallites composing (d) LATPnf and (e) pLATPnf. (f) XRD patterns of pLATPnf and LATPnf. (($\dagger$): $LiTiPO_5$; ($\ddagger$) TiP_2O_7). (g) ^7Li MAS NMR spectra of pLATPnf and LATPnf.

than the reported one, the lower time of calcination (2 h) could have played an important role in the crystal growth, thus affecting the shape of crystalline domains.[49]

XRD patterns of both LATPnf and pLATPnf are shown in Fig. 2f. The main peaks in both samples are ascribable to the rhombohedral NASICON-like structure (space group $R\bar{3}c$) of $Li_{1.3}Al_{0.3}Ti_{1.7}(PO_4)_3$ (PDF card 00-066-0868). The absence of an Al-containing secondary phase is the first evidence of the successful aliovalent substitution of Ti^{4+} by Al^{3+}. The substitution is also confirmed by the lattice parameters, shown in Table 1, which are lower than those reported for $LiTi_2(PO_4)_3$, due to the smaller size of Al^{3+} compared to Ti^{4+}.[41] In particular, the lattice parameters measured for pLATPnf are in excellent agreement with those reported by Aono et al. for $Li_{1.3}Al_{0.3}$-$Ti_{1.7}(PO_4)_3$ stoichiometry, while for LATPnf, the c parameter is larger. Since the variation of c parameter with Al content is more important than that of a/b parameter, a higher value could suggest a slightly lower degree of substitution.[41] As shown in Fig. 2f, neither secondary phases nor impurity phases were detected in the LATPnf pattern, which thus consists of pure LATP fibers. Low intensity peaks were instead detected in the pLATPnf pattern and can be attributed to small amounts of

TiP_2O_7 and $LiTiPO_5$. They are common side products in LATP high temperature synthesis procedures, resulting both from the decomposition and incomplete reaction of starting materials.[33,50,51] $LiTiPO_5$ has a similar stoichiometry and is often considered a reaction intermediate of $LiTi_2(PO_4)_3$.[52,53]

The formation of TiP_2O_7, along with TiO_2, could be also ascribed to a partial volatilization of Li_2O during the heating process,[50] however the mild conditions used are not sufficient to cause such loss of lithium. No peaks related to $AlPO_4$ and TiO_2 were detected, in accordance with previous reports on sol–gel syntheses of LATP.[54,55] This aspect confirms the successful aliovalent substitution and suggests that no thermal decomposition of LATP structure occurred.

As reported elsewhere, the high porosity of electrospun precursor fibers is beneficial for decreasing the time and temperature of calcination.[23,28] This was also confirmed by LATPnf synthesis, which required a calcination step of 2 hours at 850 °C to achieve a pure NASICON-like phase, meaning a less severe heat treatment compared to reported studies on sol–gel synthesis of bulk LATP.[54–56]

The impurity phases detected in pLATPnf are probably related to its higher density, which requires more severe heating conditions to complete the synthesis of the final product. Increasing temperature and/or time of calcination would have surely been beneficial in terms of purity, however, as mentioned above, fibers undergo coalescence when severe heating conditions are used, leading to the complete loss of their morphology. For the sake of comparison, we decided to maintain the same heating conditions for both samples, as a trade-off between morphology and purity.

Table 1 Cell parameters of LATPnf and pLATPnf compared to $LiTi_2(PO_4)$

	a (Å), b (Å)	c (Å)
$LiTi_2(PO_4)_3$ (ref. 41)	8.512	20.858
LATPnf	8.4906(3)	20.8518(10)
pLATPnf	8.49266(18)	20.8068(7)

To investigate the lithium location within the NASICON structure, ^{7}Li MAS NMR spectra of LATPnf and pLATPnf were recorded (Fig. 2g). Spectra of both samples can be described as a combination of two components centered at −1.1 ppm with C_Q values equal to 45 kHz and 5 kHz and $\eta = 0.1$. Based on data reported by Arbi *et al.* those signals can be assigned to Li ions located at M1 and M3 sites.[37] The relative integral intensities of the components in both samples are 85 : 15, respectively. We did not observe any substantial differences between LATPnf and pLATPnf, thus the pressure does not appear to affect lithium location within the structure.

To better understand how the different phases are arranged in the pLATPnf fiber morphology, we acquired EDS maps of both LATPnf and pLATPnf and the results are displayed in Fig. 3. More in detail, Fig. 3a shows the morphology of a single LATP fiber with the corresponding mapping of the main elements, namely Al, Ti, P and O, showing that an even elemental distribution and thus a homogenous phase were obtained for the LATPnf sample. Conversely, a less uniform elemental distribution is observed in the pLATPnf one (Fig. 3b and c).

Specifically, Al and Ti content vary widely, meaning that different stoichiometry and/or phases are present in the sample, in agreement with XRD patterns.

Given that no Al-containing phase has been detected by XRD analysis, the uneven Al distribution discernible in Fig. 3b is presumably related to different degrees of aliovalent substitution of Ti^{4+} by Al^{3+}.

This is confirmed by the opposite pattern displayed for the Ti distribution in the corresponding mapping. The Al-content across the sample is greatly influenced by the density of the fibers. Fig. 3b proves that Al substitution is less significant in denser areas, where consequently, a higher Ti content is observed. Thus, less dense areas are mainly made of Al-rich LATP, whereas denser ones, which are poor in Al, presumably contain also TiP_2O_7 and $LiTiPO_5$ impurity phases. As already reported, the confined space of the fiber reduces the diffusion distance of precursor materials, thus being beneficial to achieve an even distribution of the ionic species during the calcination step.[28] This advantageous effect is minimized by some margin in the pressed areas, where fibers are often clustered, thus partially resembling the bulk material.

HAADF-STEM imaging was performed to investigate the morphology of the individual fibers, and the results are shown in Fig. 4, which displays a single LATP polycrystalline fiber, composed of small cubic-shaped crystallites as already detected by SEM imaging (Fig. 2d). Darker areas are attributed to pores formed along the fiber during the calcination step. A small cluster of fibers, isolated from the pLATPnf sample, has also been investigated (Fig. 4b). Crystalline domains are less evident here, probably due to the larger thickness of the cluster compared to single fibers. No dark spots are observed in the analysis, proving that the pressure applied before the calcination step affects both intra-fiber and inter-fiber porosity. Fig. 4c shows a HRTEM image acquired on the border of a LATPnf
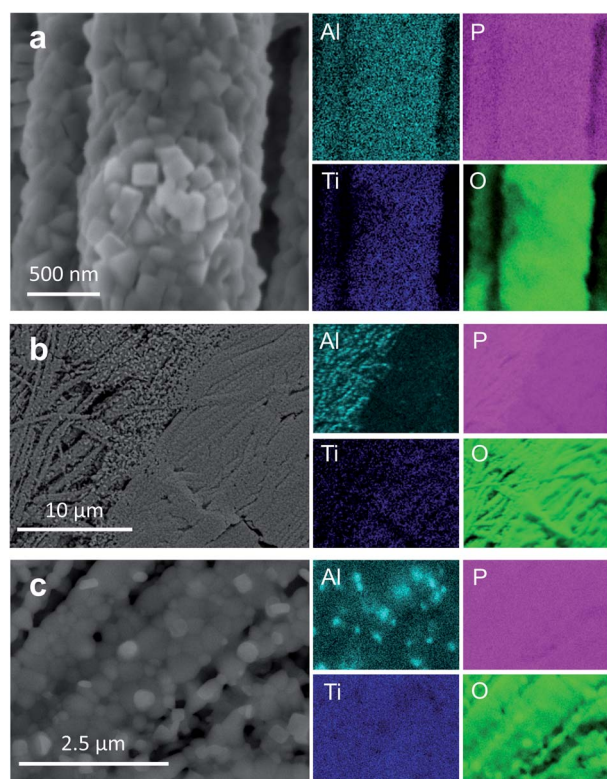

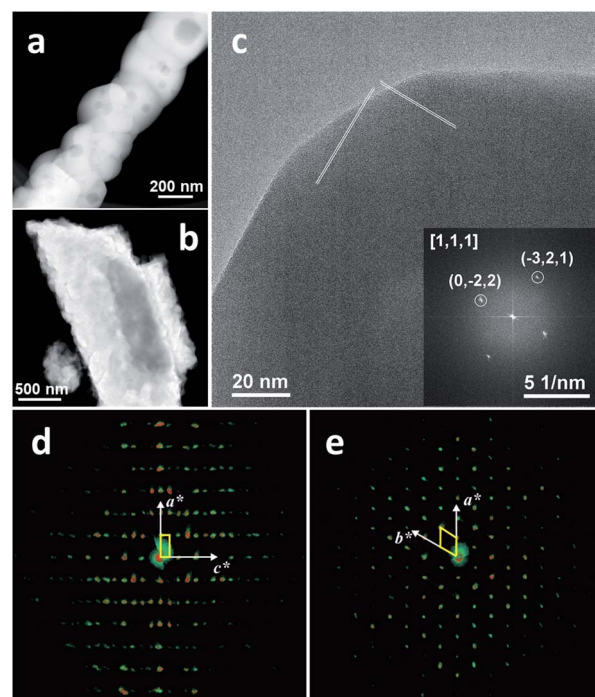Fig. 3 SEM-EDS analysis and corresponding elemental mapping of (a) LATPnf and (b and c) pLATPnf.

Fig. 4 HAADF-STEM image of (a) an isolated fiber of LATPnf and (b) a cluster of fibers of pLATPnf. (c) HRTEM image of a crystallite close to [1, 1, 1] orientation and corresponding FFT image (inset). Reconstruction of a 3D ED data set projected along (d) *b** and (e) *c**. Projections of the reciprocal vectors are sketched in white and cell edges are sketched in yellow. Extinctions *okl*: *l* = 2*n* are due to the *c*-glide plane.

crystallite. The good crystallinity for the whole sample as observed by XRD is here confirmed within a single grain. The fast Fourier transform (FFT) pattern (inset in Fig. 4c) shows the reflections corresponding to the [1, 1, 1] orientation of the NASICON structure.

Three-dimensional electron diffraction data, displayed in Fig. 4d and e, confirmed a rhombohedral structure. No reflection indicating lattice modulation was observed. Extinctions were consistent with the $R\bar{3}c$ space group. Crystal structure solution confirmed the model reported by Aono et al.,[41] based on a framework of TiO_6 octahedra and PO_4 tetrahedra. Potentials likely corresponding to Li atoms in position $6b$ (0, 0, 0) were clearly visible in the ab initio solution.

XPS spectra were acquired to further explore the elemental composition of LATP fibers. Survey spectra of LATPnf and pLATPnf samples (Fig. 5a) show the presence of the base elements, i.e. Ti, Al, P and O. Al doping in LATPnf sample corresponds to the desired stoichiometry, since the ratio of the atomic concentrations of Al and Ti is close to 1 : 5, while a 2 : 5 ratio results from pLATPnf analysis. Since XPS provides quantitative information of the sample's surface composition, the higher Al : Ti ratio observed for pLATPnf could result from the uneven elemental distribution already observed during the EDS

analysis. This unevenness is presumably related to the pressure step which locally increased the density of the sample. The higher density hinders the substitution of Ti^{4+} by Al^{3+}, causing the presence of Al-free impurity phases, i.e. TiP_2O_7 and $LiTiPO_5$. Accordingly, less dense areas are richer in Al (Fig. 5c). High-resolution spectra of Al 2p and Ti 2p are displayed in Fig. 5b. As expected, Al 2p spectra show only one peak at a binding energy of $\sim$74 eV.[57] For both samples the Ti 2p spectrum shows two evident peaks. Each of them has been deconvoluted into two peaks. Those at higher binding energy, centered at $\sim$460 eV and $\sim$466 eV, correspond to Ti^{4+} $2p_{3/2}$ and Ti^{4+} $2p_{1/2}$ respectively.[58,59] At lower binding energies, i.e. $\sim$463 eV and $\sim$458 eV, two small peaks can be attributed to Ti^{3+}.[58,59] According to the intensity of the peaks, in both samples the amount of Ti^{3+} was about 10% and presumably originates from the surface reduction of Ti^{4+} to Ti^{3+} by reducing gases produced during the calcination step.[59] Since we did not further anneal, Ti^{3+} formed during calcination does not oxidize back to Ti^{4+}.[59]

EIS analysis of both LATPnf and pLATPnf samples was performed to measure the ionic conductivity. Each sample was placed in a coin cell between stainless steel blocking electrodes (Fig. 6a) and EIS data have been acquired at a temperature ranging from 20 °C to 80 °C. The fitting of EIS spectra was performed by using the equivalent circuit depicted in Fig. 6b. The resulting total impedance was used to calculate the ionic conductivity of both samples at different temperatures, displayed as Arrhenius plot in Fig. 6d. The slope of the Arrhenius plots has been used to calculate the activation energy of both LATPnf and pLATPnf, yielding 0.37 ± 0.02 eV and 0.19 ± 0.02 eV respectively. Both results are in good agreement with the values reported in the literature for LATP.[33,55,60–62] The lowest value of pLATPnf could be related to the locally higher degree of Al substitution as well as to the better connection between LATP grains.[63–65] Regarding the ionic conductivity, LATPnf sample showed a value equal to 5×10^{-7} S cm^{-1} at 25 °C, which is slightly higher than the one reported by Lancel et al.[33] The pressure applied to pLATPnf proved to be highly beneficial for the ionic conductivity of the final electrolyte. Because of the higher density and the increased number of contact points, the pLATPnf sample is characterized by a two order of magnitude higher ionic conductivity at 25 °C, i.e. 3×10^{-5} S cm^{-1}. Four-point probe measurements were acquired to rule out a potential electronic contribution to the total conductivity due to the presence of Ti^{3+} (Fig. 5b). The data shows that the electronic conductivity of pLATPnf is negligible when compared to the total conductivity of the sample (Fig. S2†). Equivalent measurements on LATPnf were not possible as this sample is not mechanically suitable for testing with this technique (Fig. S3†). Al-rich LATP areas and $LiTiPO_5$ impurity phases could play a role in enhancing LATP's ionic conductivity. Al contents higher than 0.3 indeed proved to be beneficial for the ionic transport, as showed by both computational methods and single crystal impedance studies.[65,66] Additionally, Hupfer et al. reported that a 5% addition of $LiTiPO_5$ improves LATP's conductivity of almost one order of magnitude.[67] The direct ion conduction pathways provided by the fiber morphology, the numerous fiber contact points due to the pressing step and the
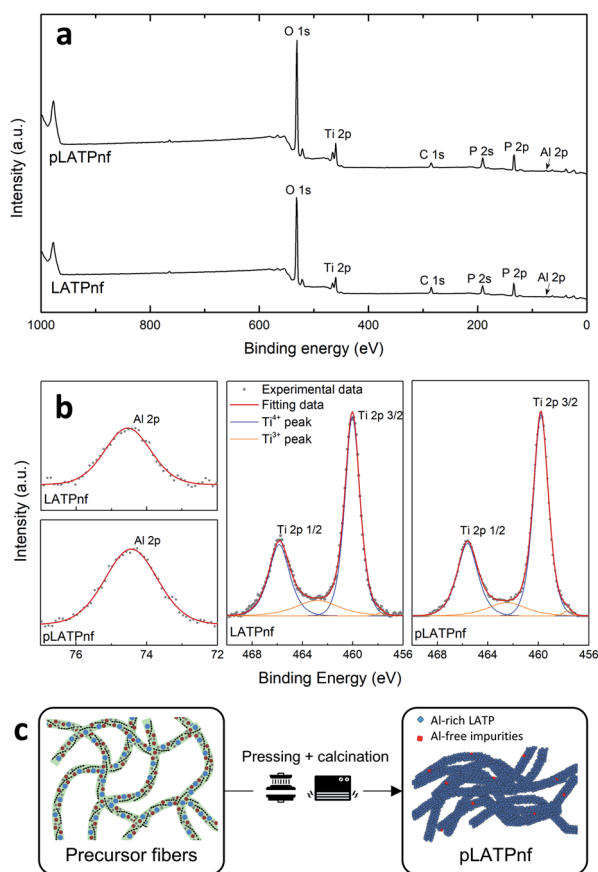

Fig. 5 (a) XPS survey spectra of LATPnf and pLATPnf samples. (b) High resolution spectra of Al 2p and Ti 2p regions. (c) Schematic illustration of the effect of the pressure on the Al content and distribution in pLATPnf.
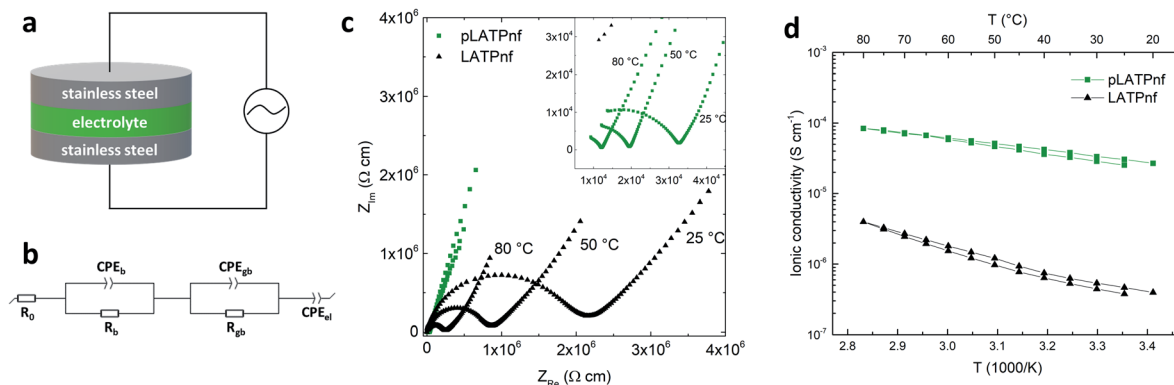
Fig. 6 (a) Scheme of the EIS analysis setup. (b) Equivalent circuit used to fit EIS data. (c) EIS spectra of LATPnf and pLATPnf at 25 °C, 50 °C and 80 °C; a magnification of pLATPnf high frequency data is shown in the inset. (d) Arrhenius plot comparing LATPnf and pLATPnf ionic conductivities in the 20–80 °C temperature range. Two consecutive scans in opposite directions have been performed.

potential contribution of impurity phases resulted in a more effective Li-ion transport in pLATPnf. Li ions are not restricted to move inside a single fiber as mostly happens in LATPnf sample, but they can hop more frequently between fibers leading to a more efficient conducting mechanism.

Conclusions and perspectives

LATP nanofibers have been synthesized by electrospinning and subsequent calcination at 850 °C for 2 h. A 150 MPa pressure was applied on the pristine membrane, prior to the calcination step, and the effects on the properties of the final sample have been investigated. The morphological characterization of LATPnf and pLATPnf samples showed that the density of the pristine membrane affects crystal growth during the calcination step. Different crystal shapes and sizes were detected in the pLATPnf sample as well as some impurity phases. These last evidences correlate with an uneven substitution of Ti with Al along pLATPnf sample. Whereas, Ti and Al contents are constant in LATPnf, they vary with the density by moving along the pLATPnf surface. Although the high porosity, typical of electrospun materials, proved to be beneficial for decreasing temperatures and times of calcination, the lower value measured for pLATPnf could be responsible for the impurity phases and the uneven elemental distribution. The higher density, coupled with the mild calcination conditions, presumably hinders the homogeneous diffusion of ions during crystal growth. Al ions appeared to be particularly affected by the local density of the sample, giving rise to Al-rich areas as well as Al-free impurity phases.

Even though the pressing step negatively affected the purity and homogeneity of LATP, it proved to be very beneficial for ionic transport across the solid electrolyte. The presence of impurity phases as well as the decrease of porosity (from 86% to 60%) led to a two order of magnitude higher ionic conductivity. The pLATPnf sample displayed a conductivity value equal to 3×10^{-5} S cm^{-1} at room temperature, which is only one order of magnitude lower than the one reported for bulk LATP. Despite this, LATPnf and pLATPnf are not suitable to be tested in

a solid-state battery configuration, since their performance will not be comparable to that of a dense LATP pellet. However, the results achieved are promising for future application of NASICON fibers as both a base for developing ceramic electrolytes and an active filler/scaffold for composite polymer electrolytes. The mild conditions that allowed to achieve a pure and homogenous NASICON phase, compared to the synthesis of bulk materials by sol–gel processes, confirmed the beneficial effect of the high porosity and the fiber morphology. Most importantly the great influence that the applied pressure and thus the density of the precursor material have on the crystal growth can be, in our view, a significant contribution to the optimization of soft-chemistry methods (*e.g.* sol–gel, Pechini, hydrothermal), which aim to develop synthesis processes featuring less severe calcination steps, and thus more suitable for industrial upscale.

Conflicts of interest

There are no conflicts to declare.

Acknowledgements

References

1 J.-W. Jung, C.-L. Lee, S. Yu and I.-D. Kim, *J. Mater. Chem. A*, 2016, **4**, 703–750.
2 L. Mai, L. Xu, C. Han, X. Xu, Y. Luo, S. Zhao and Y. Zhao, *Nano Lett.*, 2010, **10**(11), 4750–4755.
3 C. Zhu, Y. Yu, L. Gu, K. Weichert and J. Maier, *Angew. Chem., Int. Ed.*, 2011, **50**, 6278–6282.
4 J. Bell, R. Ye, K. Ahmed, C. Liu, M. Ozkan and C. S. Ozkan, *Nano Energy*, 2015, **18**, 47–56.

5 Y. Zhao, X. Li, L. Dong, B. Yan, H. Shan, D. Li and X. Sun, *Int. J. Hydrogen Energy*, 2015, **40**, 14338–14344.

6 C. Li, C. Liu, W. Wang, J. Bell, Z. Mutlu, K. Ahmed, R. Ye, M. Ozkan and C. S. Ozkan, *Chem. Commun.*, 2016, **52**, 11398–11401.

7 W. Li, M. Li, K. R. Adair, X. Sun and Y. Yu, *J. Mater. Chem. A*, 2017, **5**, 13882–13906.

8 J. Nunes-Pereira, C. M. Costa and S. Lanceros-Mendez, *J. Power Sources*, 2015, **281**, 378–398.

9 A. La Monaca, F. De Giorgio, M. L. Focarete, D. Fabiani, M. Zaccaria and C. Arbizzani, *J. Electrochem. Soc.*, 2017, **164**, A6431–A6439.

10 M. A. Spencer and V. Augustyn, *J. Mater. Sci.*, 2019, **54**, 13045–13069.

11 J. Deng, H. Ji, C. Yan, J. Zhang, W. Si, S. Baunack, S. Oswald, Y. Mei and O. G. Schmidt, *Angew. Chem., Int. Ed.*, 2013, **52**, 2326–2330.

12 Y. Chen, L. Liu, J. Xiong, T. Yang, Y. Qin and C. Yan, *Adv. Funct. Mater.*, 2015, **25**, 6701–6709.

13 J.-M. Tarascon and M. Armand, *Nature*, 2001, **414**, 359–367.

14 M. Armand and J.-M. Tarascon, *Nature*, 2008, **451**, 652–657.

15 D. Lin, Y. Liu and Y. Cui, *Nat. Nanotechnol.*, 2017, **12**, 194–206.

16 X. Shen, Y. Li, T. Qian, J. Liu, J. Zhou, C. Yan and J. B. Goodenough, *Nat. Commun.*, 2019, **10**, 900.

17 A. La Monaca, A. Paolella, A. Guerfi, F. Rosei and K. Zaghib, *Electrochem. Commun.*, 2019, **104**, 106483.

18 W. Liu, N. Liu, J. Sun, P.-C. Hsu, Y. Li, H.-W. Lee and Y. Cui, *Nano Lett.*, 2015, **15**, 2740–2745.

19 W. Liu, S. W. Lee, D. Lin, F. Shi, S. Wang, A. D. Sendek and Y. Cui, *Nat. Energy*, 2017, **2**, 17035.

20 L. Zhu, P. Zhu, Q. Fang, M. Jing, X. Shen and L. Yang, *Electrochim. Acta*, 2018, **292**, 718–726.

21 P. Zhu, C. Yan, M. Dirican, J. Zhu, J. Zang, R. K. Selvan, C.-C. Chung, H. Jia, Y. Li, Y. Kiyak, N. Wu and X. Zhang, *J. Mater. Chem. A*, 2018, **6**, 4279–4285.

22 K.-Q. He, J.-W. Zha, P. Du, S. H.-S. Cheng, C. Liu, Z.-M. Dang and R. K. Y. Li, *Dalton Trans.*, 2019, **48**, 3263.

23 T. Yang, J. Zheng, Q. Cheng, Y.-Y. Hu and C. K. Chan, *ACS Appl. Mater. Interfaces*, 2017, **9**, 21773–21780.

24 Z. Wan, D. Lei, W. Yang, C. Liu, K. Shi, X. Hao, L. Shen, W. Lv, B. Li, Q.-H. Yang, F. Kang and Y.-B. He, *Adv. Funct. Mater.*, 2019, **29**, 1805301.

25 Y. Zhao, J. Yan, W. Cai, Y. Lai, J. Song, J. Yu and B. Ding, *Energy Storage Mater.*, 2019, **23**, 306–313.

26 M. Jing, H. Yang, C. Han, F. Chen, L. Zhang, X. Hu, F. Tu and X. Shen, *J. Electrochem. Soc.*, 2019, **166**, A3019–A3027.

27 Y. Li, W. Zhang, Q. Dou, K. W. Wong and K. M. Ng, *J. Mater. Chem. A*, 2019, **7**, 3391.

28 T. Yang, Y. Li and C. K. Chan, *J. Power Sources*, 2015, **287**, 164–169.

29 S. Panero, B. Scrosati, M. Wachtler and F. Croce, *J. Power Sources*, 2004, **129**, 90–95.

30 L. Ji, Z. Lin, M. Alcoutlabi and X. Zhang, *Energy Environ. Sci.*, 2011, **4**, 2682–2699.

31 V. Augustyn, J. Come, M. A. Lowe, J. W. Kim, P.-L. Taberna, S. H. Tolbert, H. D. Abruña, P. Simon and B. Dunn, *Nat. Mater.*, 2013, **12**, 518–522.

32 T. Yang, Z. D. Gordon, Y. Li and C. K. Chan, *J. Phys. Chem. C*, 2015, **119**, 14947–14953.

33 G. Lancel, P. Stevens, G. Toussaint, M. Marechal, N. Krins, D. Bregiroux and C. Laberty-Robert, *Langmuir*, 2017, **33**, 9288–9297.

34 K. He, P. Xie, C. Zu, Y. Wang, B. Li, B. Han, M. Z. Rong and M. Q. Zhang, *RSC Adv.*, 2019, **9**, 4157–4161.

35 J. C. Bachman, S. Muy, A. Grimaud, H.-H. Chang, N. Pour, S.-F. Lux, O. Paschos, F. Maglia, S. Lupart, P. Lamp, L. Giordano and Y. Shao-Horn, *Chem. Rev.*, 2016, **116**, 140–162.

36 S. Chen, K. Wen, J. Fan, Y. Bando and D. Golberg, *J. Mater. Chem. A*, 2018, **6**, 11631.

37 K. Arbi, W. Bucheli, R. Jiménez and J. Sanz, *J. Eur. Ceram. Soc.*, 2015, **35**, 1477–1484.

38 Z.-Y. Kou, Y. Lu, C. Miao, J.-Q. Li, C.-J. Liu and W. Xiao, *Rare Met.*, 2021, DOI: 10.1007/s12598-020-01678-w.

39 Z. Kou, C. Miao, P. Mei, Y. Zhang, X. Yan, Y. Jiang and W. Xiao, *Ceram. Int.*, 2020, **46**, 9629–9636.

40 C. -S. Yang, K. -N. Gao, X. -P. Zhang, Z. Sun and T. Zhang, *Rare Met.*, 2018, **37**, 459–472.

41 H. Aono, E. Sugimoto, Y. Sadaoka, N. Imanaka and G.-Y. Adachi, *J. Electrochem. Soc.*, 1990, **137**, 1023–1027.

42 E. Mugnaioli, T. Gorelik and U. Kolb, *Ultramicroscopy*, 2009, **109**, 758–765.

43 M. Gemmi, E. Mugnaioli, T. E. Gorelik, U. Kolb, L. Palatinus, P. Boullay, S. Hovmöller and J. P. Abrahams, *ACS Cent. Sci.*, 2019, **5**, 1315–1329.

44 U. Kolb, E. Mugnaioli and T. E. Gorelik, *Cryst. Res. Technol.*, 2011, **46**, 542–554.

45 M. C. Burla, R. Caliandro, B. Carrozzini, G. L. Cascarano, C. Cuocci, C. Giacovazzo, M. Mallamo, A. Mazzone and G. Polidori, *Appl. Crystallogr.*, 2015, **48**, 306–309.

46 W. Xiao, J. Wang, L. Fan, J. Zhang and X. Li, *Energy Storage Mater.*, 2019, **19**, 379–400.

47 X. Shi, N. Ma, Y. Wu, Y. Lu, Q. Xiao, Z. Li and G. Lei, *Solid State Ionics*, 2018, **325**, 112–119.

48 E. Yi, K. Yoon, H. Jung, T. Nakayama, M. Ji and H. Hwang, *Appl. Surf. Sci.*, 2018, **7**, 622–626.

49 K. G. Schell, E. C. Bucharsky, F. Lemke and M. J. Hoffmann, *Ionics*, 2017, **23**, 821–827.

50 Z. Luo, C. Qin, W. Xu, H. Liang, W. Lei, X. Shen and A. Lu, *Ceram. Int.*, 2020, **46**, 15163–15620.

51 R. Kahlaoui, K. Arbi, R. Jimenez, I. Sobrados, J. Sanz and R. Ternane, *J. Mater. Sci.*, 2020, **55**, 8464–8476.

52 A. Robertson, J. G. Fletcher, J. M. Skakle and A. R. West, *J. Solid State Chem.*, 1994, **109**, 53–59.

53 T. Hupfer, E. C. Bucharsky, K. G. Schell, A. Senyshyn, M. Monchak, M. J. Hoffmann and H. Ehrenberg, *Solid State Ionics*, 2016, **288**, 235–239.

54 Y. Liang, Z. Lin, Y. Qiu and X. Zhang, *Electrochim. Acta*, 2011, **56**, 6474–6480.

55 E. C. Bucharsky, K. G. Schell, A. Hintennach and M. J. Hoffmann, *Solid State Ionics*, 2015, **274**, 77–82.

56 M. Kotobuki and M. Koishi, *Ceram. Int.*, 2013, **39**, 4645–4649.

57 P. Bhanja, C. Senthil, A. K. Patra, M. Sasidharan and A. Bhaumik, *Microporous Mesoporous Mater.*, 2017, **240**, 57–64.

58 T. Yang, X. Liu, L. Sang and F. Ding, *J. Power Sources*, 2013, **244**, 43–49.

59 B. V. R. Chowdari, G. V. Subba Rao and G. Y. H. Lee, *Solid State Ionics*, 2000, **136–137**, 1067–1075.

60 S. Wang, L. Ben, H. Li and L. Chen, *Solid State Ionics*, 2014, **268**, 110–116.

61 M. Monchak, T. Hupfer, A. Senyshyn, H. Boysen, D. Chernyshov, T. Hansen, K. G. Schell, E. C. Bucharsky, M. J. Hoffmann and H. Ehrenberg, *Inorg. Chem.*, 2016, **55**, 2941–2945.

62 S. Breuer, D. Prutsch, Q. Ma, V. Epp, F. Preishuber-Pflügl, F. Tietz and M. Wilkening, *J. Mater. Chem. A*, 2015, **3**, 21343.

63 K. Arbi, S. Mandal, J. M. Rojo and J. Sanz, *Chem. Mater.*, 2002, **14**(3), 1091–1097.

64 M. Pérez-Estébanez, J. Isasi-Marín, D. M. Többens, A. Rivera-Calzada and C. León, *Solid State Ionics*, 2014, **266**, 1–8.

65 B. Zhang, Z. Lin, H. Dong, L.-W. Wang and F. Pan, *J. Mater. Chem. A*, 2020, **8**, 342.

66 D. Rettenwander, A. Welzl, S. Pristat, F. Tietz, S. Taibl, G. J. Redhammer and J. Fleig, *J. Mater. Chem. A*, 2016, **4**, 1506.

67 T. Hupfer, E. C. Bucharsky, K. G. Schell and M. J. Hoffmann, *Solid State Ionics*, 2017, **302**, 49–53.